Chapter 2

Fluctuations of the Energy Flux in Wave Turbulence

S. Aumaître*, E. Falcon†,§ and S. Fauve‡

*SPEC, DSM, CEA-Saclay, CNRS,
91 191 Gif-sur-Yvette, France

†Université Paris Diderot, Sorbonne Paris Cité,
MSC, UMR 7057, CNRS, F-75 013 Paris, France

‡LPS, ENS Paris, CNRS, 24 rue Lhomond, 75 005 Paris, France
§eric.falcon@univ-paris-diderot.fr

The key governing parameter of wave turbulence is the energy flux that drives the waves and cascades to small scales through nonlinear interactions. In the inertial range, the energy flux is conserved across the scales, and is assumed to be constant in most theoretical approaches. It is only recently that measurements of the injected power into wave turbulence have been performed at the scale of the wave maker (integral scale). In this review, we focus on the statistical properties of the injected power fluctuations in gravity-capillary wave turbulence in a stationary regime. Fluctuations of the injected power have been found much larger than their mean value. In addition, events related to a negative injected power, i.e. an instantaneous reversed energy flux, occur with a fairly large probability. Both features are well described using a Langevin type equation. Finally, we consider the experimental dependence of the scaling law of the wave spectrum with the mean injected power and discuss possible reasons for the discrepancy with weak turbulence theory.

Contents

2.1. Introduction

A fundamental problem of wave turbulence consists of describing the transfer of energy among different scales through the weak interaction between waves. It was understood first by Zakharov (1967) that the kinetic equations obtained in the weak turbulence limit have stationary solutions that involve a finite mean energy flux per unit surface and density ϵ across the scales. In the case of a n-wave process, the energy spectrum of the wave heights $E(k)$ is proportional to $\epsilon^{1/(n-1)}$. Once this is taken into account, the power-law dependence of $E(k)$ on the wavenumber k often follows from dimensional analysis (Connaughton *et al.*, 2003),

$$E(k) \propto \epsilon^{1/(n-1)} k^{\alpha}, \tag{2.1}$$

where the proportionality constant involves parameters of the dispersion relation. Since measurements are often performed in time at a fixed point in space, it is useful to consider an equation similar to (2.1) in the frequency domain

$$E(\omega) \propto \epsilon^{1/(n-1)} \omega^{\beta}. \tag{2.2}$$

In weak turbulence theory, Eqs. (2.1) and (2.2) are related through the dispersion relation $\omega = W(k)$. This has been checked only recently by comparison of the spatial and temporal spectra determined in experiments of waves on elastic plates (Cobelli *et al.*, 2009) and capillary-gravity surface waves (Snouck *et al.*, 2009; Herbert *et al.*, 2010). A fair agreement has been found in the former case whereas a more complex structure in the spatio-temporal domain exists in the latter ones. Most of the experiments performed so far have dealt with the determination of the exponents α and β related to the spatial (respectively temporal) spectrum. Although a fair agreement with theory has been often claimed, detailed measurements show disagreement in many cases: for elastic waves on plates (see the chapter by N. Mordant) or gravity waves for which the spectrum has been shown to depend on the amplitude and frequency content of the forcing (Falcon *et al.*, 2007a; Denissenko *et al.*, 2007; Nazarenko *et al.*, 2010). The spectrum of capillary waves looks more robust, an exponent in rough agreement with theory being found in different configurations, high frequency part of surface waves (Falcon *et al.*, 2007a), pure capillary waves observed in microgravity (Falcon *et al.*, 2009), and capillary waves at the interface between two fluids with similar density (Düring and Falcón, 2009).

It is thus of primary interest to test other predictions of the weak turbulence theory in order to determine its range of validity. Measuring the dependence of the spatial (respectively temporal) spectrum on the mean

energy flux ϵ is the next step. No direct measurement of the energy flux within the inertial range exists so far, but its mean value is equal to the mean injected power of the force driving the system. That quantity can be measured. We will discuss these measurements in Sec. 2.3.

A second aspect concerns the fluctuations of the energy flux. It has been known for a long time that the power needed to maintain a dissipative system in a statistically stationary regime is generally a fluctuating quantity. This has been shown in the case of spatio-temporally chaotic waves generated by the Faraday instability (Ciliberto *et al.*, 1991), hydrodynamic turbulence (Labbé *et al.*, 1996) and many other dissipative systems such as granular gases (Aumaître *et al.*, 2001, 2004). However, very few general results have been obtained so far about the properties of the fluctuations of global quantities in dissipative systems driven far from equilibrium. In all these systems, dissipative processes damp out any initial motion in the absence of an external forcing. In order to reach a statistically stationary regime, an external operator should provide an injected power $I(t)$ that, on average, compensates the dissipation $D(t)$. The equation for the energy budget takes the form

$$\frac{dE(t)}{dt} = I(t) - D(t), \tag{2.3}$$

where E is an energy, for instance the kinetic energy of a turbulent flow or of a granular gas. In majority of the situations, the external operator never controls one of the global quantities, I, D or E. It usually drives the system by imposing locally a given force or velocity, for instance, the velocity or the torque applied to a propeller generating a turbulent flow, or the vibration velocity of a piston driving waves in a fluid or motions of the particles in a granular gas. The injected power $I(t)$ is thus generally a fluctuating quantity, that can often take instantaneous negative values depending on the phase of the response of the system to the driving (Aumaître *et al.*, 2001). It should be positive on average, since we have in a statistically stationary regime

$$\langle I \rangle = \langle D \rangle, \tag{2.4}$$

with $D(t) > 0$ in a macroscopic description of a dissipative system. Equation (2.3) is probably one of the most common equations of physics since it only states that the time variation of some quantity results from the difference between input and output. It is thus surprising that its general properties have not been emphasized more often. In a statistically stationary regime, Eq. (2.4) is of course well known, but to the best of our knowledge, this is not the case for the relations involving higher moments of the fluctuations of $I(t)$ and $D(t)$. For instance, $I(t)$ and $D(t)$ should have

the same spectrum at zero frequency (Aumaître *et al.*, 2004; Farago, 2004)

$$|\hat{I}(0)|^2 = |\hat{D}(0)|^2, \tag{2.5}$$

or using Wiener–Kintchine theorem,

$$\int_0^\infty [\langle I(\tau)I(0)\rangle - \langle I\rangle^2]d\tau = \int_0^\infty [\langle D(\tau)D(0)\rangle - \langle D\rangle^2]d\tau. \tag{2.6}$$

If the correlation functions decay fast enough at large τ, the above equation shows that the variances of the injected and dissipated power are related by

$$\sigma_I^2\tau_I = \sigma_D^2\tau_D, \tag{2.7}$$

where τ_I (respectively τ_D) is the correlation time of $I(t)$ (respectively $D(t)$). As explained by Aumaître *et al.* (2004) and Farago (2004), the above results trace back to the large deviation functions for I and D that have the same Taylor expansion about $\langle I\rangle = \langle D\rangle$.

This chapter is organized as follows: first, we recall experimental results about gravity-capillary surface waves in a turbulent regime and show how the spectra depend on the injected power in the system. Then, we consider the fluctuations of the injected power and their statistical properties. We show that the experimental observations can be modeled using a Langevin-type equation driven by colored noise.

2.2. Spectra in the Gravity and Capillary Regimes

The experimental setup is shown in Fig. 2.1. It consists of a square plastic vessel, 20 cm side, filled with a fluid up to a depth $h = 1.8$ or 2.3 cm leading to an almost deep water limit ($\lambda \lesssim 2\pi h$ for our range of wavelengths λ). Mercury is chosen as the working fluid because of its low kinematic viscosity (one order of magnitude smaller than that of water), thus reducing wave dissipation. Note, however, that similar qualitative results to the ones reported here are found when changing mercury by water. The properties of mercury are, density $\rho = 13.5\ 10^3\,\mathrm{kg/m^3}$, kinematic viscosity $\nu = 1.15\ 10^{-7}\,\mathrm{m^2/s}$ and surface tension $\gamma = 0.4\,\mathrm{N/m}$. Surface waves are generated by the horizontal motion of two rectangular ($10 \times 3.5\,\mathrm{cm^2}$) plunging Plexiglas wave makers driven by two electromagnetic vibration exciters. The wave makers are driven with a random noise (in amplitude and frequency) band-pass filtered within a frequency bandwidth between 1 Hz and f_p (f_p being typically from $f_p = 4$ to 6 Hz). This corresponds to wavelengths of surface waves larger than 4 cm. The height η of the surface waves is measured at a given location (7 cm away from the wave makers) by a capacitive wire gauge plunging perpendicularly to the fluid surface at rest. The latter is made of an

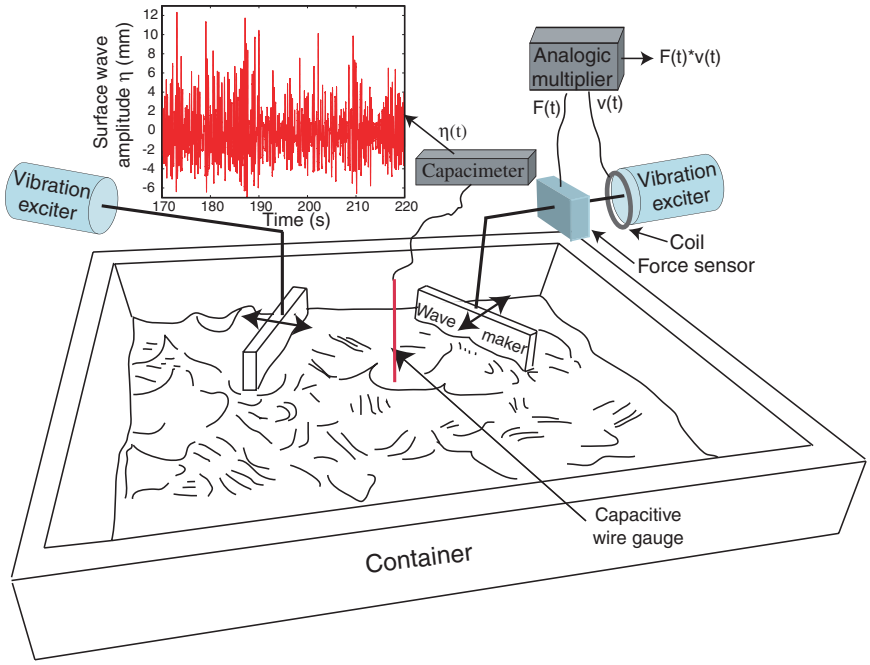

Fig. 2.1. Schematic view of the experimental setup showing a typical time recording of the surface wave height, $\eta(t)$, at a given location during 50 s. $\langle\eta\rangle \simeq 0$.

insulated copper wire, 0.1 mm in diameter, the insulation (a varnish) being the dielectric of an annular capacitor with the wire as the inner conductor and mercury as the outer one. The capacitance is thus proportional to the fluid level. A low-cost home-made analogic multivibrator with a response time 0.1 ms is used as a capacitance meter in the range 0–200 pF. The linear sensing range of the sensor allows wave height measurements from 10 μm up to 2 cm with a 20 mm/V sensitivity. We have checked that the exact location of the capacitive sensor has almost no influence on the wave spectrum. Note that the maximum forcing amplitude is less than the onset of the water drop ejection or wave breaking.

A typical recording of the surface wave amplitude, $\eta(t)$, at a given location is displayed in the inset of Fig. 2.1 as a function of time. The wave amplitude is very erratic with a large distribution of amplitudes. The largest values of the amplitude are of the order of the fluid depth, whereas the mean value of the amplitude is close to zero. The asymmetry of the fluctuations (larger crests than troughs) is stronger when the height of the layer is smaller but it persists in the deep layer limit (Falcon *et al.*, 2007a).

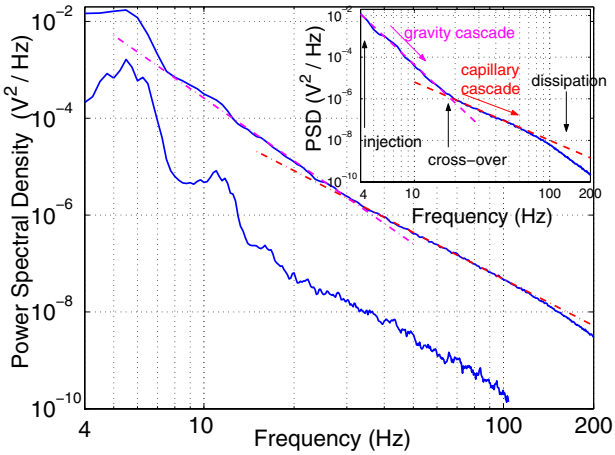

Fig. 2.2. Power spectra of the surface wave height for two different injected powers $\langle I \rangle = 1.6$ and 32.4 mW (from bottom to top). Dashed-dotted lines have slopes -4.3 and -3.2. Random forcing within a 1–6 Hz frequency bandwidth. Inset: Same with $\langle I \rangle = 32.4$ mW and a 1–4 Hz bandwidth. Dashed lines have slopes -6.1 and -2.8.

The power spectrum density of the wave height,

$$S_\eta(f) \equiv \int \langle \eta(t+\tau)\eta(t) \rangle_t \mathrm{e}^{-i2\pi f \tau} d\tau,$$

is recorded using a spectrum analyzer from 4 Hz up to 200 Hz and averaged during 2000 s. For a small forcing, peaks related to the forcing and its harmonic are visible in the low frequency part of the spectrum in Fig. 2.2. At a higher forcing, those peaks are smeared out and a power-law can be fitted. At higher frequencies, the slope of the spectrum changes, and a crossover is observed near 20 Hz between two regimes. This corresponds to the transition from gravity to capillary wave turbulence. For a narrower frequency band of excitation (1–4 Hz), similar spectra are found but with a broader power-law in the gravity range (see inset of Fig. 2.2).

For linear waves, the crossover between gravity and capillary regimes corresponds to a wave number k of the order of the inverse of the capillary length $l_c \equiv \sqrt{\gamma/(\rho g)}$, i.e. to a critical frequency, $f_c = \sqrt{g/2l_c}/\pi$, where g is the acceleration of gravity. For mercury, $l_c = 1.74$ mm and $f_c \simeq 17$ Hz corresponding to a wavelength of the order of 1 cm. The inset of Fig. 2.2 shows a correct agreement in the case of a narrow driving frequency band. We also observe that the crossover frequency increases with the driving amplitude and with the width of the driving frequency band (Falcon *et al.*, 2007a). This can be due to the fact that the above estimate of f_c is only valid for linear waves.

Surface wave turbulence is usually described as a continuum of interacting waves governed by kinetic-like equations in the case of small nonlinearity and weak wave interactions. Weak turbulence theory predicts that the surface height spectrum $S_\eta(f)$, i.e. the Fourier transform of the autocorrelation function of $\eta(t)$, is scale invariant with a power-law frequency dependence. Such a Kolmogorov-like spectrum writes

$$S_\eta(f) \propto \epsilon^{\frac{1}{2}} \left(\frac{\gamma}{\rho}\right)^{\frac{1}{6}} f^{-\frac{17}{6}} \quad \text{for capillary waves}$$

(Zakharov and Filonenko, 1967a)

$$S_\eta(f) \propto \epsilon^{\frac{1}{3}} g f^{-4} \quad \text{for gravity waves (Zakharov and Filonenko, 1967b),} \tag{2.8}$$

where ϵ is the energy flux per unit surface and density [$S_\eta(f)$ has dimension L^2T and ϵ has dimension $(L/T)^3$]. In both regimes, these frequency power-law exponents are compared with the slopes of surface height spectra measured for different forcing intensities and bandwidths. The experimental values of the scaling exponent of capillary spectra are close to the expected $f^{-2.8}$ scaling as already shown with one driving frequency (Wright *et al.*, 1996; Lommer and Levinsen, 2002; Brazhnikov, Kolmakov and Levchenko, 2002) or with noise (Brazhnikov, Kolmakov and Levchenko, 2002). However, in these previous works, peaks and their harmonics (related to the parametric forcing) are observed on the spectrum with maximal amplitudes decreasing as a frequency power-law (Snouck *et al.*, 2009; Brazhnikov, Kolmakov and Levchenko 2002; Brazhnikov *et al.*, 2002). The frequency-spectrum exponent estimated in that way is thus not very accurate. A recent study has even found an exponent in disagreement with weak turbulence underlying the difficulty to reach a wave turbulence regime with a parametric forcing (Snouck *et al.*, 2009). In the case of our measurements, we observe that this exponent for the capillary range does not depend on the amplitude and the frequency band of the forcing, within our experimental precision. For the gravity spectrum, no power-law is observed at a small forcing since the turbulence is not strong enough to hide the first harmonic of the forcing (see Fig. 2.2). At high enough forcing, the scaling exponent of gravity spectra is found to increase with the intensity and the frequency band from -6 to -4 such that the predicted f^{-4} scaling of Eq. (2.8) is only observed for the largest forcing intensities and bandwidth (Falcon *et al.*, 2007a). The dependence of the slope of the gravity waves spectrum on the forcing characteristics has been ascribed to finite size effects (Falcon *et al.*, 2007a). Similar results in the gravity range have been found in a much larger tank with sinusoidal forcing

(Denissenko *et al.*, 2007; Nazarenko *et al.*, 2010). This dependence has been also ascribed to the presence of strong nonlinear waves (Cobelli *et al.*, 2011). However, recent experiments have shown that it is related to the anisotropy and inhomogeneity of the forcing (Issenmann and Falcon, 2013).

2.3. Direct Measurement of the Injected Power

The power injected into the fluid by the wave maker is determined as follows. The velocity $V(t)$ of the wave maker is measured using a coil placed on the top of the vibration exciter (see Fig. 2.1). The voltage induced by the moving permanent magnet of the vibration exciter is proportional to $V(t)$. The force $F_A(t)$ applied by the vibration exciter on the wave maker is measured by a piezoresistive force transducer (FGP 10 daN). $F_A(t)$ and $V(t)$ recorded by means of an acquisition card with a 1 kHz sampling rate during 300 s. The time recordings of $V(t)$ and $F_A(t)$ together with their PDFs are displayed in Fig. 2.3. Both $V(t)$ and $F_A(t)$ are Gaussian with zero mean value. For a given excitation bandwidth, the rms value σ_V of

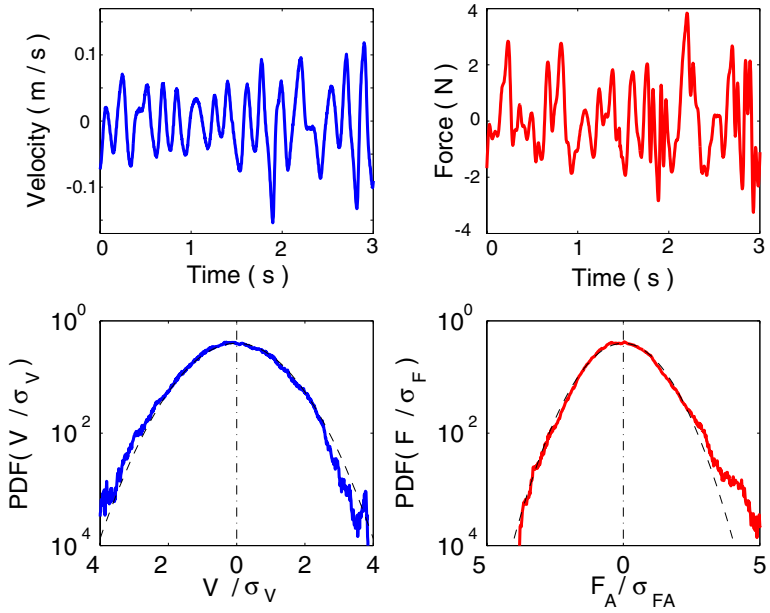

Fig. 2.3. Time recordings of the velocity of the wave maker and the force applied to the wave maker by the vibration exciter ($\langle F_A \rangle \approx \langle V \rangle \approx 0$). The fluid is mercury, with $h = 23$ mm. Both PDFs are Gaussian (dashed lines) with zero mean value.

the velocity fluctuations of the wave maker is proportional to the driving voltage U applied to the electromagnetic shaker and does not depend on the fluid density ρ. On the contrary, the standard deviation σ_{F_A} of the force applied to the wave maker is decreased by the density ratio (~ 13) when mercury is replaced by water. The rms velocity of the wave maker is thus prescribed in our experiments. We have checked that $\sigma_{F_A} \propto \rho \mathcal{S} \sigma_V$ where $\mathcal{S}$ is the immersed area of the wave maker. This linear behavior has been measured on one decade up to $\sigma_{F_A} \sim 2$ N and $\sigma_V \sim 0.1\,\mathrm{m/s}$. The power injected into the fluid by the wave maker is $I(t) = -F_R(t)V(t)$ where $F_R(t)$ is the force applied by the fluid on the wave maker. It generally differs from $F_A(t)V(t)$ which is measured here, because of the piston inertia (see below). However, their time averages are equal, thus $\langle I \rangle = \langle F_A(t)V(t) \rangle$.

The mean energy flux ϵ is estimated by the measurement of $\langle I \rangle / (\rho \mathcal{S})$ where $\langle I \rangle$ is the mean power injected by the wave maker and $\mathcal{S}$ is the immersed area of the wave maker. With given σ_V, we have first checked that $\langle I \rangle$ is proportional to $\mathcal{S}$ and decreases by a factor 13 when mercury is replaced by water. Our measurements also show that $\langle I \rangle \propto \sigma_V^2$ with a proportionality coefficient of order $10\,\mathrm{W/(m/s)^2}$ (see the inset of Fig. 2.4). We thus have $\epsilon \propto c\sigma_V^2$ where c has the dimension of a velocity. If we assume that ϵ should involve only large scale quantities, it cannot depend

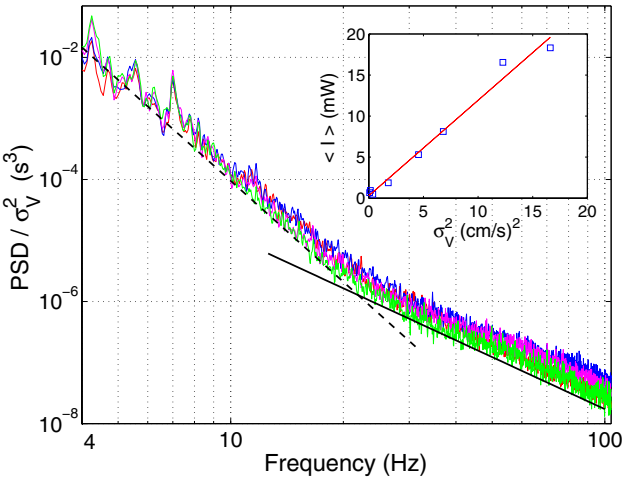

Fig. 2.4. Spectra of the surface wave height divided by the variance σ_V^2 of the velocity of the wave maker for different forcing amplitudes, $\sigma_V = 2.1, 2.6, 3.5$ and $4.1\,\mathrm{cm/s}$. Random forcing with a 1–4 Hz frequency bandwidth. The dashed line has slope -5.5 whereas the full line has slope $-17/6$. The mean injected power is displayed as a function of σ_V^2 in the inset. The best fit gives a slope $11.5\,\mathrm{W/(m/s)^2}$.

on surface tension or viscosity. Then, we need an additional length scale or time scale besides g in order to be able to determine c. In a deep fluid range, the height of the layer h cannot be used and the additional parameter could be the horizontal size of the layer or equivalently the travel time of the large scale gravity waves. Without this additional parameter, we should get $\epsilon \propto \sigma_V^3$ as usually assumed in weak turbulence theory. The dependence of ϵ on c can be ascribed to finite size effects. The inverse of travel time of a wave within the tank or the frequency difference between the discrete modes of the tank, both scale with c. Note that the peaks are visible at low frequencies in the spectrum of Fig. 2.2 at low forcing amplitude. Discreteness also explains the presence of these peaks that correspond to vessel eigenvalue modes (Deike *et al.*, 2012). However, the large enough values of ϵ required to observe power-laws, are more than one order of magnitude smaller than the critical flux $(\gamma g/\rho)^{3/4} \approx 2200\,(\mathrm{cm/s})^3$ corresponding to the breakdown of weak turbulence (Newell and Zakharov, 1992).

We consider now how the spectra of the gravity and capillary waves scale with the mean energy flux. The best choice in order to collapse our experimental spectra on a single curve for different values of σ_V is displayed in Fig. 2.4 where the power spectral density divided by σ_V^2 is plotted versus f. Surprisingly, spectra are collapsed on both the gravity and capillary ranges by this single scaling. The wave height spectrum is found to scale as $\langle I\rangle^{1\pm0.1}$ for both gravity and capillary wave turbulence regimes over almost one decade in $\langle I\rangle$ as shown in Fig. 2.4. This scaling does not depend on the vessel geometry when using a circular one of similar size. A similar spectrum scaling $\sim \langle I\rangle^1$ has been observed for both regimes by horizontally vibrating the whole container (Issenmann and Falcon, 2013) for the same range of $\langle I\rangle$, for the capillary regime with a parametric forcing (Xia *et al.*, 2010), and for the inverse cascade of gravity wave turbulence (Deike *et al.*, 2011). Moreover, it has been checked that $\langle I\rangle \sim \sigma_\eta^2$, where σ_η is the rms value of the wave height. This is coherent with $S_\eta(f) \sim \langle I\rangle^1$ (Issenmann and Falcon, 2013) since $\int_0^\infty S_\eta(f)df = \sigma_\eta^2/(2\pi)$.

Another way to estimate the mean energy flux consists of measuring the wave energy decay rate after switching off the wave maker (Denissenko *et al.*, 2007; Nazarenko *et al.*, 2010). This method gives a good estimate of the mean energy flux provided large scale dissipation is negligible. Measurements performed in Deike *et al.* (2012) show that the decay rate does not depend on the initial wave amplitude, thus giving a capillary spectrum scaling in ϵ^1 instead of the predicted $\epsilon^{1/2}$ one. This shows that the large scale waves lose most of their energy through large scale dissipation and not by transferring energy to smaller scales.

Thus, both the scaling of the mean injected power $\langle I \rangle \sim \sigma_V^2$ with respect to the forcing velocity σ_V and the linear scaling of the spectrum $S_\eta(f) \sim \langle I \rangle^1$ are in disagreement with the weak turbulence theory that predicts a spectrum $\sim \epsilon^{1/3}$ in the gravity regime and $\sim \epsilon^{1/2}$ in the capillary regime (see above). Note also that matching the gravity regime to the capillary one using Eq. (2.8) gives a crossover frequency that slightly decreases when ϵ is increased whereas an increase with ϵ is observed. This also shows a discrepancy with respect to weak turbulence theory that is likely to be related to the previous ones but does not require the measurement of $\langle I \rangle$.

We now discuss some possible reasons for the discrepancy between the experimental measurements presented above and the theory of weak turbulence. We first consider the measurements involving the injected power. A first possibility is that one part of the power is directly provided to the bulk flow and dissipated by viscosity without cascading through the wave field. For instance, the wave maker can generate vortices that would dissipate some part of the injected power. Although this mechanism is certainly present, it is unlikely to be the dominant one. Indeed, as said above, the scaling laws involving the mean injected power do not change when the forcing is made by horizontally vibrating the whole container instead of using wave makers. In addition, $\langle I \rangle \propto \sigma_V^2$ would correspond to the Stokes regime whereas the Reynolds number of the wave maker is larger than 1000 in mercury.[1] Thus, we rather think that most of the injected power is transferred to large scale waves. A second possibility to explain the observed discrepancy is that, although chaotic (a broad band spectrum is observed at large enough forcing), these large scale waves transfer a small amount of energy flux to higher harmonics compared to their direct dissipation by viscosity. This speculation is strengthened by recent experiments of decaying wave turbulence on the surface of a fluid that have shown that only a small part of the initial power injected into the waves feeds the capillary cascade, whereas the major part is dissipated at large scales (Deike *et al.*, 2012). For stationary wave turbulence, it is thus likely that only some fraction of the power injected into waves cascades through the scales, the rest being dissipated at various scales. This unknown dissipated fraction of injected power could be at the origin of the discrepancy with weak turbulence theory for the scaling of the spectrum with the injected power. This can also explain the discrepancies that do not involve the measurement of the mean energy flux. It is likely that finite size

[1]For a typical wave maker forcing (0.4 cm amplitude and 4 Hz frequency), its velocity is 0.1 m/s, and its Reynolds number is 4000 in mercury ($\nu = 10^{-7}\,\mathrm{m}^2/\mathrm{s}$).

effects, by inhibiting the energy transfers among large scale waves, prevent the observation of a cascade regime in the gravity range with the scaling predicted by weak turbulence theory (Falcon *et al.*, 2007a). The presence of strong fluctuations of the injected power (see Sec. 2.4) can also affect the predictions of the theory. This issue is still open and deserves more studies. For instance, it will be of primary interest to measure the energy flux at various scales (instead of the injected power by the wave maker) by a fully resolved space–time measurement.

2.4. Fluctuations of the Energy Flux

We now study the fluctuations of the power injected by the wave maker in the fluid. When the wave maker inertia is negligible, the power $I(t)$ injected into the fluid is roughly given by $F_A(t)V(t)$ (see below). The time recording of $I(t)$ is shown in the inset of Fig. 2.5. Contrary to the velocity or the force, the injected power consists of strong intermittent bursts. Although the forcing is statistically stationary, there are quiescent periods with a small amount of injected power interrupted by bursts where $I(t)$ can take both positive and negative values. The PDFs of $I/\langle I\rangle$ are displayed in Fig. 2.5. They show that the most probable value of I is zero and display two asymmetric exponential tails (or stretched exponential in the smaller

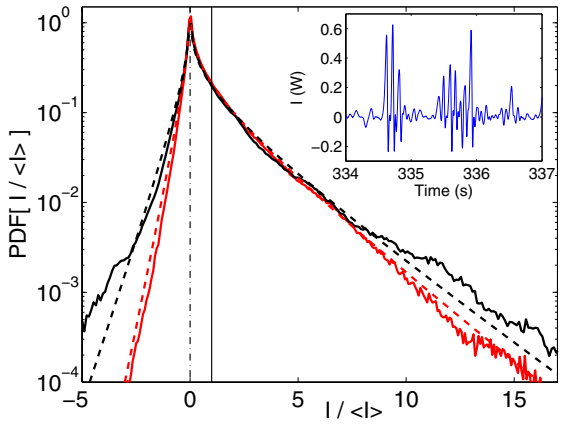

Fig. 2.5. PDF of $I(t)/\langle I\rangle$ for mercury: $\sigma_V = 5\,\mathrm{cm/s}$, container size $57 \times 50\,\mathrm{cm}^2$ [red (light grey)] and $20 \times 20\,\mathrm{cm}^2$ (black) ($h = 18\,\mathrm{mm}$). Red (light grey) solid line: experiment with $\langle I\rangle = 51\,\mathrm{mW}$ and $\sigma_{F_A} = 1.6$ N. Black solid line: experiment with $\langle I\rangle = 2\,\mathrm{mW}$ and $\sigma_{F_A} = 0.73$ N. Dashed lines are the related predictions from Eq. (2.12) without fitting parameter, $r = 0.7$ [red (light grey)] and $r = 0.6$ (black). Vertical solid line show the mean injected power. Inset: time recording of $I(t)$.

container). We observe that events with $I(t) < 0$, i.e. for which the wave field gives back energy to the wave maker, occur with a fairly high probability. The standard deviation σ_I of the injected power is much larger than its mean value $\langle I \rangle$ and rare events with amplitude up to $7\sigma_I$ are also detected.

We also observe in Fig. 2.5 that the probability of negative events strongly decreases when the container size is increased whereas the positive fluctuations are less affected. This shows that the backscattering of the energy flux from the wave field to the driving device is related to the waves reflected by the boundary that can, from time to time, drive the wave maker in phase with its motion. We note that we have less statistics for the negative tail of the PDF when the size of the container is increased.

We emphasize the bias that can result from the system inertia when one tries a direct measurement of the fluctuations of injected power. The equation of motion of the wave maker is

$$M\dot{V} = F_A(t) + F_R(t), \tag{2.9}$$

where M is the mass of the wave maker and $F_R(t)$ is the force due to the fluid motion. The power injected into the fluid by the wave maker is $I(t) = -F_R(t)V(t)$. When $M\dot{V}$ is not negligible, $I(t)$ generally differs from $F_A(t)V(t)$ which is experimentally determined. This obviously does not affect the mean value $\langle I \rangle$ but may lead to wrong estimates of the fluctuations. Using an accelerometer, we have checked that $M\dot{V}$ is negligible compared to F_A when the working fluid is mercury. On the contrary, inertia cannot be neglected for experiments in water for which an error as large as one order of magnitude can be made on the probability of rare events if one use $F_A V$ to estimate I. Thus, the correction due to $M\dot{V}$ has been taken into account in water experiments.

The PDF of injected power for the same driving in the same container for mercury displays a larger asymmetry than the one for water. This is related to the larger mean energy flux, i.e. mean dissipation, for mercury, as shown below.

The qualitative features of the PDF of injected power can be described with the following simple model. Guided by our experimental observation of the linearity of σ_{F_A} in σ_V (see Sec. 2.3), we assume that the force F_R due to the fluid can be roughly approximated by a friction force $-M\gamma V$, where γ is a constant (the inverse of the damping time of the wave maker). We are aware that a better approximation to the force due to the fluid should involve both $\dot{V}$ and an integral of $V(t)$ with an appropriate kernel. Thus, we only claim here to give a heuristic understanding of the qualitative properties of the PDF of I. Since in our experiment the forcing is stochastic and low-pass filtered at frequency $1/\beta$, we model the forcing with an

Ornstein–Uhlenbeck process:

$$\dot{V} = -\gamma V + F, \quad \dot{F} = -\beta F + \xi, \tag{2.10}$$

where β is the inverse of the correlation time of the applied force ($F = F_A/M$) and ξ is a Gaussian white noise with $\langle \xi(t)\xi(t')\rangle = \Delta\delta(t-t')$. The PDF $P(V,F)$ is the bivariate normal distribution (Risken, 1996)

$$P(V,F) = \frac{\exp\left[-\frac{1}{2(1-r^2)}\left(\frac{V^2}{\sigma_V^2} - \frac{2rVF}{\sigma_V\sigma_F} + \frac{F^2}{\sigma_F^2}\right)\right]}{2\pi\sigma_V\sigma_F\sqrt{1-r^2}}, \tag{2.11}$$

with $\sigma_F = \sqrt{\Delta/2\beta}$, $\sigma_V = \sqrt{\Delta/(2\gamma\beta(\gamma+\beta))}$ and $r = \sqrt{\gamma/(\gamma+\beta)}$. Changing variables (V,F) to $(\tilde{I} = FV = I/M, F)$ and integrating over F gives

$$P(\tilde{I}) = \frac{\exp\left[\frac{r\tilde{I}}{(1-r^2)\sigma_V\sigma_F}\right]}{\pi\sigma_V\sigma_F\sqrt{1-r^2}} K_0\left[\frac{|\tilde{I}|}{(1-r^2)\sigma_V\sigma_F}\right], \tag{2.12}$$

where $K_0(X)$ is the zeroth-order modified Bessel function of the second kind. Using the method of steepest descent, this predicts exponential tails, $P(X) \sim (1/\sqrt{|X|})\exp(rX - |X|)$ where $X = \tilde{I}/[(1-r^2)\sigma_V\sigma_F]$. In addition, we have $\langle\tilde{I}\rangle = \Delta/[2\beta(\gamma+\beta)] = r\sigma_V\sigma_F$. Thus, (2.12) is determined once $\langle I\rangle$, σ_V and σ_F have been measured and can be compared to the experimental PDF without using any fitting parameter. This is displayed with dashed lines in Fig. 2.5. Taking into account the strong approximation made in the above model, we observe a good agreement in the larger container. More importantly, this model captures the qualitative features of the PDF: its maximum for $I = 0$ and the asymmetry of the tails that is governed by the parameter $r = \sqrt{\gamma/(\gamma+\beta)} = \langle I\rangle/(\sigma_V\sigma_{F_A})$. For given σ_V and σ_{F_A}, the larger is the mean energy flux, i.e. the dissipation, the more asymmetric is the PDF. For mercury, direct determination of r from the measurement of $\langle I\rangle$, σ_V and σ_{F_A} gives $r \sim 0.7$ for the large container and $r \sim 0.6$ for the small one. Smaller values of r are achieved in water for which the dissipation is smaller. The PDFs are more stretched for water, in particular, in the smaller container.

In order to explain this modification of the PDF, we consider the effect of nonlinearities in the model, for instance, in the form of a velocity-dependent damping term, $\gamma(V) = \frac{\gamma_o}{1+aV^2}$, in (2.10). The weaker damping at large velocity does generate stretched exponential tails in the PDF of injected power with more probable large events as shown in Fig. 2.6. However, the PDF of the velocity is no longer Gaussian in that case (inset of Fig. 2.6).

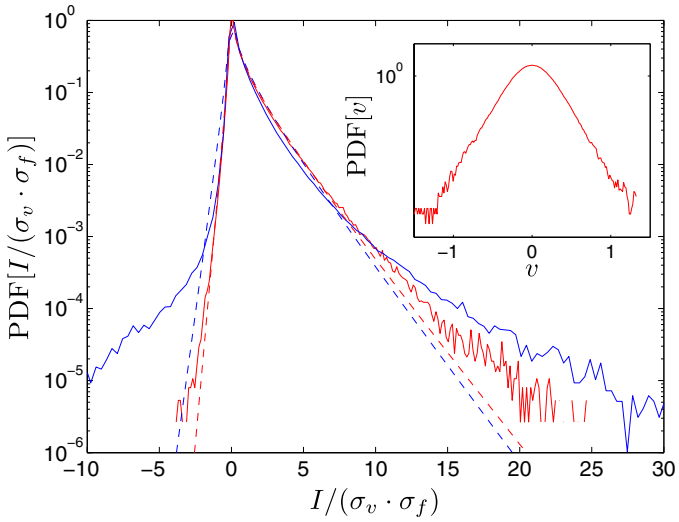

Fig. 2.6. PDF of the injected power from the numerical resolution of Eq. (2.10) with a nonlinear damping coefficient $\gamma(V) = \frac{\gamma_o}{1+aV^2}$ with $\gamma_o = 1$, $\beta = 0.5$, $\sigma_f = 0.22$: $a = 1.0$ (red) and $a = 2.0$ (blue). Dashed lines correspond to Eq. (2.12) for the same values of $\langle I \rangle$, σ_V, and σ_{F_A}. Inset: PDF of the velocity for $a = 1.0$.

One could notice that the PDF of I given by (2.12) respects a symmetry similar to the one of the fluctuation theorem (Evans *et al.*, 1993; Gallavotti and Cohen, 1995), but without any time averaging. Indeed, we get

$$\frac{1}{\tau_F} \log \frac{P(I)}{P(-I)} = \frac{2}{\sigma_V^2} I, \tag{2.13}$$

where $\tau_F = 1/\beta$ is the correlation time of the force. Thus, $\sigma_V^2/2$ plays the role of an effective temperature, $k_B T = \sigma_V^2/2$.

However, the symmetry related to the fluctuation theorem is not observed with our data if we consider, as we should, the injected power averaged on a time interval τ

$$I_\tau(t) = \frac{1}{\tau} \int_t^{t+\tau} I(t')dt'. \tag{2.14}$$

The PDFs of I_τ for $\tau/\tau_c = 1, 3, 11$ and 50 where τ_c is the correlation time of $I(t)$, are displayed in Fig. 2.7. They become more and more peaked around $I_\tau \simeq \langle I \rangle$, as they should. However, one needs to average on a rather large time interval ($\tau \sim 50\tau_c$) in order to get a maximum probability $P(I_\tau)$

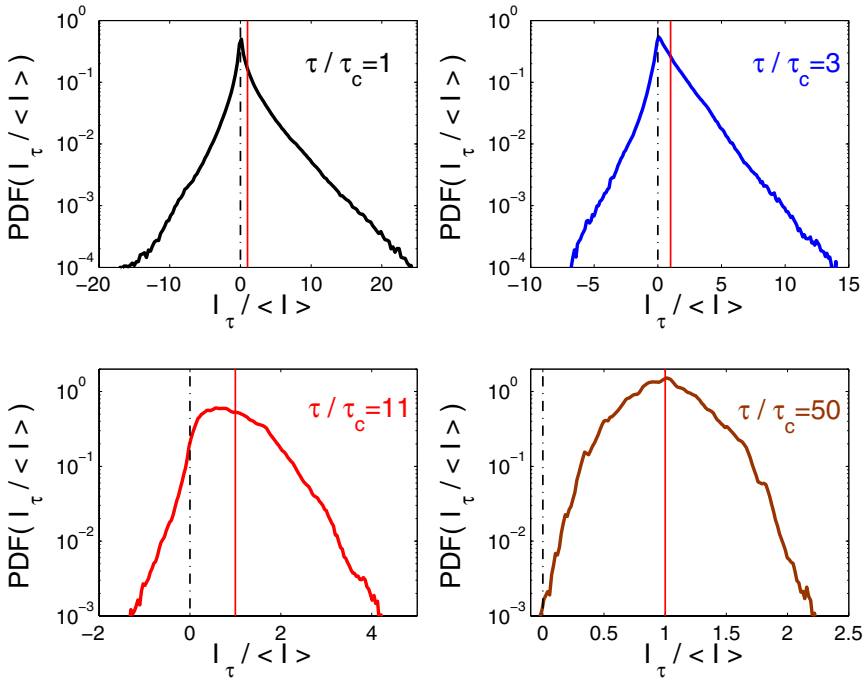

Fig. 2.7. PDFs of the injected power I_τ averaged on a time interval τ: $\tau = 1, 3, 11$ and $50\tau_c$, where $\tau_c = 0.03\,\mathrm{s}$ is the correlation time of $I(t)$. Solid lines indicate the value of $\langle I \rangle$ (water, $h = 23\,\mathrm{mm}$).

for $I_\tau = \langle I \rangle$ (Fig. 2.7, bottom right). Then, the probability of negative events become so small that almost none can be observed. Figure 2.8 shows that the quantity $\frac{1}{\tau} \log \frac{P(I_\tau/\langle I \rangle)}{P(-I_\tau/\langle I \rangle)}$ for different values of τ that has been predicted to be linear in $I_\tau/\langle I \rangle$ for $\tau \gg \tau_c$ when the hypotheses of the fluctuation theorem (in particular time reversibility) are fulfilled (Evans *et al.*, 1993; Gallavotti and Cohen, 1995; Kurchan, 1998). As we clearly observe in Fig. 2.8, this is not the case in general for macroscopic (i.e. energy $\gg kT$) dissipative systems. As already mentioned (Aumaître *et al.*, 2001) and studied in detail (Puglisi *et al.*, 2005; Visco *et al.*, 2005), the linear behavior reported in several experiments or numerical simulations results from the too small values of $I_\tau/\langle I \rangle$ that are probed when $\tau \gg \tau_c$. Large enough values are obtained in the present experiment and the expected nonlinear behavior is thus reached. The shape of the curve in Fig. 2.8 is found in good agreement with the analytical calculation (Farago, 2002) performed with a Langevin-type equation with white noise.

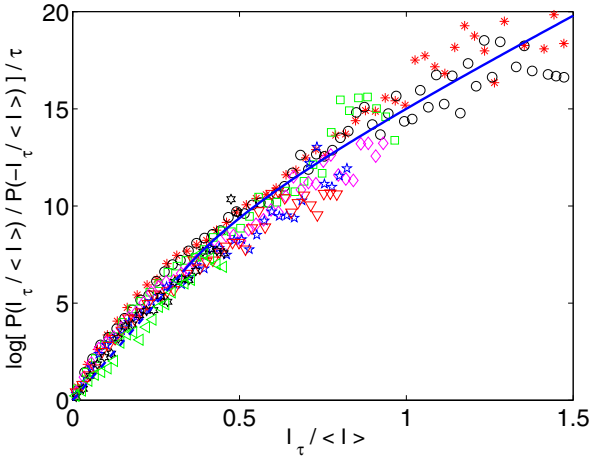

Fig. 2.8. Plot of $\frac{1}{\tau}\log\frac{P(I_\tau/\langle I\rangle)}{P(-I_\tau/\langle I\rangle)}$ for $16 < \tau/\tau_c < 39$ [$\tau/\tau_c = 17$ ($*$), 19.5 ($\circ$), 22 ($\square$), 25 ($\Diamond$), 28 (pentagram), 30.5 (∇), 33.5 (hexagram), 39 ($\triangleleft$)]. Langevin model of Farago (2002): 4γ for $I_\tau/\langle I\rangle \leq 1/3$ (dashed line) and $7\gamma I_\tau/(4\langle I\rangle) + 3\gamma/2 - \gamma\langle I\rangle/(4I_\tau)$ for $I_\tau/\langle I\rangle \geq 1/3$ (solid line) with $\gamma = 5\,\mathrm{Hz}$.

Finally, we emphasize that a fluctuating injected power implies fluctuations of the energy flux at all wavenumbers in the energy cascade from injection to dissipation. In any system where an energy flux cascades from the injected power at large scales to dissipation at small scales, one has for the energy $E_<$ for wavenumbers smaller than k within the inertial range, $\dot{E}_< = I(t) - \Phi(k,t) \equiv R$, where $\Phi(k,t)$ is the energy flux at k toward large wavenumbers. Thus, $\int_0^\infty \langle R(\tau)R(0)\rangle d\tau = 0$ in order to prevent the divergence of $\langle E_<^2\rangle$. Dimensionaly, this implies that $\sigma_\Phi^2\tau_k$ does not depend on k, where σ_Φ is the standard deviation of the energy flux and τ_k is its correlation time. If this dimensional scaling is correct, fluctuations of the energy flux are expected to increase during the cascade from large to small scales since τ_k decreases. Such fluctuations have been found numerically and experimentally in hydrodynamic turbulence (Cerutti and Meneveau, 1998; Tao *et al.*, 2002). To which extent this is related or modified by small scale intermittency (Falcon *et al.*, 2007a) remains an open question.

2.5. Conclusion

The key governing parameter of wave turbulence is the energy flux that drives the waves and cascades to small scales through nonlinear interactions.

This quantity is assumed to be conserved during the cascades across the scales. It is only recently that measurements of the injected power into wave turbulence systems have been performed at the scale of the wave maker (integral scale). Fluctuations of the injected power much larger than the mean value have been observed as well as instantaneous negative events that occur with a fairly large probability. Taking into account these energy flux fluctuations in theoretical models of cascades remains an open problem. Moreover, it is likely that only an unknown fraction of the power injected into the system cascades through the scales, the rest being directly dissipated at various scales. To which extent, this could explain the discrepancy with theory for the observed scaling law of the power spectrum with the injected power, is an open problem that deserves more studies. For instance, an experimental challenge is to measure the evolution of the energy flux at various scales of the cascade using fully resolved space–time measurements of wave amplitude.

Acknowledgment

This work has been supported by ANR Turbulence 12-BSO4-005.

Bibliography

Aumaître S, Fauve S, McNamara S, Poggi P. 2001. Power injected in dissipative systems and the fluctuation theorem. *Eur. Phys. J. B* 19: 449.

Aumaître S, Farago J, Fauve S, McNamara S. 2004. Energy and power fluctuations in vibrated granular gases. *Eur. Phys. J. B* 42: 255.

Brazhnikov MYu, Kolmakov GV, Levchenko AA. 2002. The turbulence of capillary waves on the surface of liquid hydrogen. *Sov. Phys JETP* 95: 447–454.

Brazhnikov MYu, Kolmakov GV, Levchenko AA, Mezhov-Deglin LP. 2002. Observation of capillary turbulence on the water surface in a wide range of frequencies. *Europhys. Lett.* 58: 510–516.

Cerutti S, Meneveau C. 1998. Intermittency and relative scaling of subgrid-scale energy dissipation in isotropic turbulence. *Phys. Fluids* 10: 928.

Ciliberto S, Douady S, Fauve S. 1991. Investigating space-time chaos in Faraday instability by means of the fluctuations of the driving acceleration. *Europhys. Lett.* 15: 23.

Cobelli P, Petitjeans P, Maurel A, Pagneux V, Mordant N. 2009. Space-time resolved wave turbulence in a vibrating plate. *Phys. Rev. Lett.* 103: 204301.

Cobelli P, Przadka A, Petitjeans P, Lagubeau G, Pagneux V, Maurel A. 2011. Different regimes for water wave turbulence. *Phys. Rev. Lett.* 107: 214503.

Connaughton C, Nazarenko S, Newell AC. 2003. Dimensional analysis and weak turbulence. *Physica D* 184: 86–97.

Deike L, Laroche C, Falcon E. 2011. Experimental study of the inverse cascade in gravity wave turbulence. *Europhys Lett.* 96: 34004.

Deike L, Berhanu M, Falcon E. 2012. Decay of capillary wave turbulence. *Phys. Rev. E.* 85: 066311.

Denissenko P, Lukaschuk S, Nazarenko S. 2007. Gravity wave turbulence in a laboratory flume. *Phys. Rev. Lett.* 99: 014501.

Düring G, Falcón C. 2009. Symmetry induced Four-wave capillary wave turbulence. *Phys. Rev. Lett.* 103: 174503.

Evans DJ, Cohen EGD, Morriss GP. 1993. Probability of second law violations in shearing steady states. *Phys. Rev. Lett.* 71: 2401.

Falcon E, Laroche C, Fauve S. 2007. Observation of gravity-capillary wave turbulence. *Phys. Rev. Lett.*, 98: 094503.

Falcon E, Fauve S, Laroche C. 2007. Observation of intermittency in wave turbulence. *Phys. Rev. Lett.* 98: 154501.

Falcón C, Falcon E, Bortolozzo U, Fauve S. 2009. Capillary wave turbulence on a spherical fluid surface in zero gravity. *Europhys Lett.* 86: 14002.

Farago J. 2002. Injected power fluctuations in Langevin equation. *J. Stat. Phys.* 107: 781.

Farago J. 2004. Power fluctuations in stochastic models of dissipative systems. *Physica A* 331: 69.

Gallavotti G, Cohen EGD. 1995. Dynamical ensembles in nonequilibrium statistical mechanics. *Phys. Rev. Lett.* 74: 2694.

Herbert E, Mordant N, Falcon E. 2010. Observation of the nonlinear dispersion relation and spatial statistics of wave turbulence on the surface of a fluid. *Phys. Rev. Lett.* 105: 144502.

Issenmann B, Falcon E. 2012. Gravity wave turbulence revealed by horizontal vibrations of the container. *Phys. Rev.* E 87:011001(R).

Kurchan J. 1998. Fluctuation theorem for stochastic dynamics. *J. Phys. A* 31: 3719.

Labbé R, Pinton JF, Fauve S. 1996. Power fluctuations in turbulent swirling flows. *J. Phys II France* 6: 1099.

Lommer M, Levinsen MT. 2002. Using laser-induced fluorescence in the study of surface wave turbulence. *J. Fluoresc.* 12: 45–50.

Nazarenko S, Lukaschuk S, McLelland S, Denissenko P. 2010. Statistics of surface gravity wave turbulence in the space and time domains. *J. Fluid Mech.* 642: 6902080.

Newell AC, Zakharov VE. 1992. Rough sea foam. *Phys. Rev. Lett.* 69: 1149–1151.

Puglisi A, *et al.* 2005. Fluctuations of internal energy flow in a vibrated granular gas. *Phys. Rev. Lett.* 95: 110202.

Risken H. 1996. *The Fokker-Planck Equation.* Berlin: Springer-Verlag.

Snouck D, Westra M-T, van de Water W. 2009. Turbulent parametic surface waves. *Phys. Fluids* 21: 025102.

Tao B, Katz J, Meneveau C. 2002. Statistical geometry of subgrid-scale stresses determined from holographic particle image velocimetry measurements, *J. Fluid Mech.* 457: 35.

Visco P, *et al.* 2005. Injected power and entropy flow in a heated granular gas. *Europhys Lett.* 72: 55.

Wright WB, Budakian R, Putterman SJ. 1996. Diffusing light photography of fully developed isotropic ripple turbulence. *Phys. Rev. Lett.* 76: 4528–4531.

Xia H, Shats M, Punzmann H. 2010. Modulation instability and capillary wave turbulence. *Europhys Lett.* 91: 14002.

Zakharov VE. 1967. Weak turbulence in media with a decay spectrum. *J. Appl. Mech. Tech. Phys.* 6(4): 22–24.

Zakharov VE, Filonenko NN. 1967. Weak turbulence of capillary waves. *J. App. Mech. Tech. Phys.* 8: 37–40.

Zakharov VE, Filonenko NN. 1967. Energy spectrum for stochastic oscillations of the surface of a liquid. *Sov. Phys. Dokl.* 11: 881–884.